Hindawi
Advances in Materials Science and Engineering
Volume 2021, Article ID 6614381, 16 pages
https://doi.org/10.1155/2021/6614381

Research Article

Design and Numerical Simulation of Pyramidal Prefolded Patterned Thin-Walled Tubes

Junxian Zhou[1], **Chuang Dong**[1], **Bingzhi Chen**[2] and **Xu Niu**[3]

[1]*School of Materials Science and Engineering, Dalian Jiaotong University, Dalian 116028, Liaoning, China*
[2]*School of Locomotive and Rolling Stock Engineering, Dalian Jiaotong University, Dalian 116028, Liaoning, China*
[3]*School of Mechanical Engineering, Dalian Jiaotong University, Dalian 116028, Liaoning, China*

Correspondence should be addressed to Bingzhi Chen; chenbingzhi06@hotmail.com

Received 23 October 2020; Revised 24 December 2020; Accepted 6 January 2021; Published 19 January 2021

Academic Editor: José António Fonseca de Oliveira Correia

An improved pyramidal prefolded pattern was designed and applied to thin-walled tubes. This delicately designed pattern modularizes the tube to control the folding process and act as an inducer to trigger deformation modes with outstanding crushing performance. Dynamic crushing tests were conducted numerically; the simulation results reveal that the patterned square tube developed a deformation mode with shorter wavelength, better load consistencies, and higher energy-absorption efficiency (up to 29%) than that of the traditional counterpart. Moreover, geometric analysis was performed and structural improvements were conducted by applying the optimal geometric parameters onto an octagonal profile. The designed patterned octagonal tube collapsed into a highly efficient deformation mode known as diamond mode. Furthermore, the comparative results show that patterned octagonal tubes demonstrated an energy absorption up to 90.1% higher than that of a conventional square column while improving the geometric compliance. These findings enrich research on patterned tubes and provide new explorations for the development of high-performance energy-absorbing structures.

1. Introduction

Energy dissipating components, which commonly comprise metal tubes, are used to govern the passive safety of transport vehicles. A successfully designed energy absorber must exhibit three key advantages: low peak load, controllable deformation mode, and high energy-absorption efficiency.

Many pioneering researchers have employed circular [1–7] or square columns [8–11] and have focused on the crushing resistance of thin-walled structures. The collapse behaviors of these conventional structures under axial impacts have been studied both experimentally and theoretically. The classical superfolding element method was established by Wierzbicki and Abramowicz [8] and experimentally validated by Abramowicz and Jones [9, 10]; this method provides a convenient and reliable approach for analyzing and predicting the crushing resistance of thin-walled structures. Researchers then extended this theory to arbitrary multicorner elements [11, 12], thus making it possible to analyze the folding mechanism of polygonal tubes. The energy-absorption enhancement derived from a polygonal section has been widely confirmed; however, the defects, including the larger peak force and severe load fluctuation, are nonnegligible and thus have made polygonal tubes unsatisfactory for widespread implementation [13–16].

Various methods have been used to improve the mechanical properties of traditional tubes, including filling the tubes with foam [17–19], dividing the tube section into multicell configurations [18–22], and designing structures with functionally graded thicknesses [23–26]. Other researchers have aimed to improve the crushing response of thin-walled tubes by optimizing the crushing process. For example, Singace and El-Sobky [27] experimentally studied the effect on the mechanical responses of corrugations in aluminum and PVC circular columns, whereas Daneshi and Hosseinipour [28] investigated the effect on the axial crushing resistance of grooves on circular steel tubes. They

found that introducing corrugations or grooves helped control the folding patterns to some extent and improve load uniformity but decreased the specific energy absorption. Similar results were also observed on square columns by Lee [29].

Inspired by corrugation tubes [27–29], columns with prefolded patterns were designed [30–35], which inherited such advantages as controllable deformation mode and low peak force to improve their energy-absorbing ability. The reasons are as follows: their modular structure makes the folding process controllable; the prefolded pattern, equivalent to an initial imperfection, reduces the peak force and can induce specific deformation modes with excellent energy-absorption efficiency. For example, Zhang et al. [30] proposed introducing specific patterns on the surface of a conventional square column. They attempted two types of patterns constructed by pyramidal elements and found an efficient buckling mode, known as the octagonal mode (or diamond mode), which is, however, sensitive to the ratio of tube width to wall thickness, B/t. To trigger this efficient mode easily, Ma et al. [31] designed a square tube with diamond-shaped rigid origami patterns; this effect was then experimentally verified by Zhou et al. [32], and their results demonstrated that triggering the efficient diamond mode was difficult and that the deformation mode was very sensitive to initial defects caused by manufacturing processes. In addition, they proposed another tube design employing kite-shaped origami patterns [33], but the improvement in energy-absorption efficiency was still limited.

Generally, traditional thin-walled tubes have natural deformation modes determined by their geometric dimensions [8–12], which usually have low performance. The introduction of prefolded patterns can transform natural modes into high-performance models. However, when the target deformation mode deviates greatly from the natural mode, columns will exhibit either unstable characteristics or become sensitive to changes in their geometric parameters, thereby causing difficulties when collapsing into the expected mode [31]. This is the main reason for which the predetermined deformation modes of some existing patterned tubes failure are activated. Moreover, prior investigations on patterned columns have been mainly based on quasistatic loading but rarely on dynamic loading. The prefolded patterns, which act as initial imperfections, may weaken the dynamic amplification effect and make the crushing performance advantage of patterned tubes relative to traditional tubes under dynamic impact lower than that subjected to quasistatic loading.

In summary, improved patterned tubes with predetermined deformation modes that are easier to activate are required, and their performance advantages compared with conventional structures under dynamic loads also need to be comprehensively verified. This work therefore aims to introduce an improved pyramidal patterning onto the surface of traditional tubes with square and octagonal profiles to trigger them collapse in widely inducible and highly efficient deformation modes. Thereafter, numerical simulations are conducted to investigate the crushing resistance of the patterned tubes under dynamic impact and to explore the effects of key geometric parameters on crushing responses. The remainder of this manuscript is thus laid out as follows. Geometric designs of prefolded tubes are presented in Section 2. The patterned tubes with varying geometries and traditional tubes under study are then designed, and numerical results and geometric analyses are presented in Sections 3 and 4, respectively, followed by suggested structural improvements in Section 5. Finally, conclusions are drawn in Section 6.

2. Design of Tubes with Prefolded Patterns

The performance of square tubes subjected to axial crushing is closely related to the deformation mode. Three common modes, i.e., quasi-inextensional, extensional, and mixed as determined by the value of B/t, were theoretically investigated by Abramowicz and Jones [9, 10]. Among these three deformation modes, the extensional deformation mode was found to be the most efficient in energy absorption; however, its activation requires harsh conditions, i.e., with a value of $B/t < 7.5$ [10], which does not usually meet the requirements of structural dimensions for engineering applications.

Although the energy-absorption efficiency associated with the quasi-inextensional mode is slightly lower, its characteristics are more stable and more easily triggered. Thus, to trigger improved quasi-inextensional modes, a pattern consisting of identical basic elements was designed and applied to the surface of conventional columns. One such element is a flat-topped pyramid with width B, length l, and height h, as illustrated in Figures 1(a)–1(c), where the solid red lines in the side and top view indicate the pyramid top characterized by its width p and length s. The relationship between the top area (A_t) and the bottom area (A_b) is proportional and can be expressed as follows:

$$\frac{A_t}{A_b} = R^2, \qquad R = \frac{p}{B} = \frac{s}{l}. \tag{1}$$

The coefficient R is clarified in Figure 1(d). When $R = 0$, the pyramids have spires; when $R > 0$, the pyramids have flat tops as increasing R increases the area of the top surface. Thus, when $R = 1$, the pyramidal elements are simply flat plates.

The steepness of the pyramid can be described by any of the following parameters under constant R: the height h and the angles θ and α. These two angles can be calculated as

$$\theta = \tan^{-1}\frac{(1-R)l}{2h}, \qquad \alpha = \tan^{-1}\frac{(1-R)B}{2h} = \tan^{-1}\left(\frac{B\tan\theta}{l}\right). \tag{2}$$

A pattern was then obtained by arranging the fundamental pyramids longitudinally to form a column and then repeating it circumferentially. Adjacent columns were staggered, resulting in a height difference of $l/2$ between two circumferentially adjacent pyramids. This is illustrated by

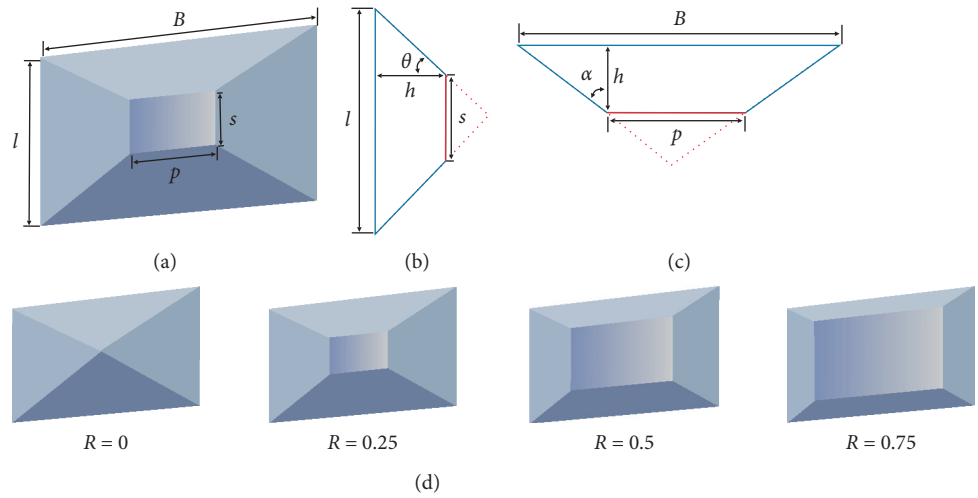

Figure 1: Basic pyramidal element: (a) overall view, (b) side view, (c) top view, and (d) different shapes caused by the change of R.

the representative tube in Figure 2(a), where M represents the number of foundational pyramids in the longitudinal direction. Thus, for the tube depicted in this figure, $M = 4$; a single module (i.e., for which $M = 1$) is depicted in Figure 2(b). The top of each pyramid pointed inwards; when combined with the dislocated arrangement of adjacent columns, this was designed to drive the tubes to crush into the quasi-inextensional mode with more folding periods than their natural modes. Under axial compression, one pair of inclined plastic hinge lines will form at each corner, denoted by orange dotted lines in Figure 2(b), provided that the predetermined deformation mode is successfully triggered.

To determine the relationship between key parameters and the energy-absorption performance of tubes patterned with the designed structures under axial compression, numerical simulations were then performed, as discussed in the following sections.

3. Numerical Simulation

Square prefolded tubes were investigated using the FEM method, which has been widely used to simulate complex nonlinear problems, including collisions [13–16, 19–31, 33], explosions [36], and even material fatigue [37]. Patterned tubes with various geometries were modeled to understand the effects of the defined feature parameters on crushing performance. Moreover, the traditional square tube (SQU) was also constructed as the benchmark for the comparative analysis. Small dent triggers were introduced below the crushed end of the traditional tube to ensure a regular and progressive buckling mode. For all tubes containing pyramidal elements, tube length $L = 220$ mm, tube width $B = 90$ mm, and thickness $t = 3.0$ mm, identical to those of SQU.

The explicit nonlinear finite element code ANSYS/LS-DYNA was used to simulate the axial crushing of tubes, during which a specimen is clamped at the bottom end and crushed from the top by a moving rigid wall with only an axial degree of freedom, as summarized in Figure 3. A prescribed crushing distance of 150 mm was assigned to the moving rigid wall to govern the impact stroke. Two types of contacts were considered in the crushing process: the automatic single-surface contact, which was introduced to simulate the self-contact of the column, and automatic surface-to-surface contact, which was applied between the column and rigid wall. The rigid wall moved at a constant velocity V of 10 m/s to investigate the response of the designed prefolded tubes under low-velocity impact. Only the contribution of the inertia effect on the dynamic effect was considered, as a strain-rate insensitive aluminum alloy, AA6060 T4, was chosen for all tubes to avoid the strain-rate effect.

The mechanical properties of AA6060 T4 include Young's modulus $E = 68.2$ GPa, Poisson's ratio $\nu = 0.3$, initial yield strength $\sigma_y = 80$ MPa, ultimate strength $\sigma_u = 173$ MPa, and power-law exponent $n = 0.23$ [17]. The stress-strain relationship is shown in Figure 4. Belytschko–Tsay quadrilateral shell elements, which are characterized by five integration points along the thickness and one integration point in the element plane, were used to model the tube and were supplemented by a few triangular elements to deal with local complex geometries and avoid abnormal elements.

Maximum peak force $P_{\max}$ and the numerical mean load P_m of each specimen were generated from the simulation results to compare the performance differences of the specimens.P_m was calculated as follows:

$$P_m = \frac{\int_0^{\delta} P(x)}{\delta}, \tag{3}$$

where δ denotes the effective crushing distance and $P(x)$ is the numerical impact load. Due to the weight discrepancy among tubes caused by their varying pattern geometries,P_m cannot effectively reflect the difference in their energy-absorption performance. Thus, the specific energy absorption (SEA), defined as the ratio of energy absorption to the tube mass m, was introduced, which can be expressed as

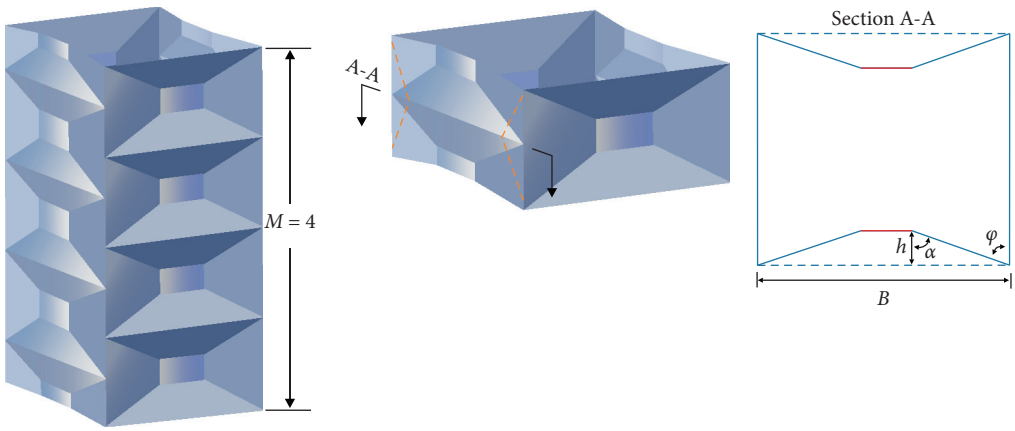

Figure 2: Geometry of the square tube with pyramidal elements: (a) square tube with $M = 4$, (b) a single module, and (c) a cross section of the module.

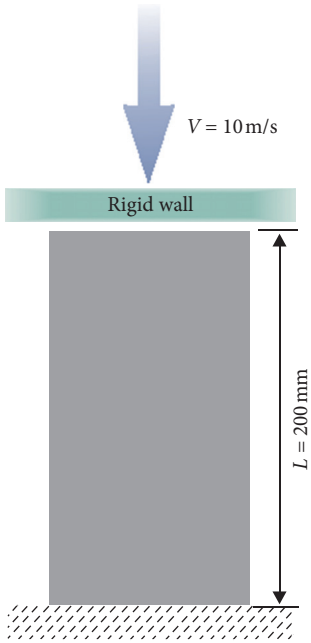

Figure 3: Schematic of the tube under axial crush.

$$\text{SEA} = \frac{P_m \delta}{m}. \tag{4}$$

Detailed physical dimensions and simulation results of the specimens under study are listed in Tables 1–3 , which were drawn for the analysis of the parameters M and θ, ratio R, and coefficient B/t, respectively. It is necessary to introduce the information and symbols presented in the tables in which the SQU and S denote the traditional square specimen and square prefolded tubes, respectively. Each prefolded tube was labeled to indicate its shape, modules present, θ, and R; for instance, specimen S3_R25_60 is a square prefolded tube with three modules for which $R = 0.25$ and $\theta = 60^\circ$.

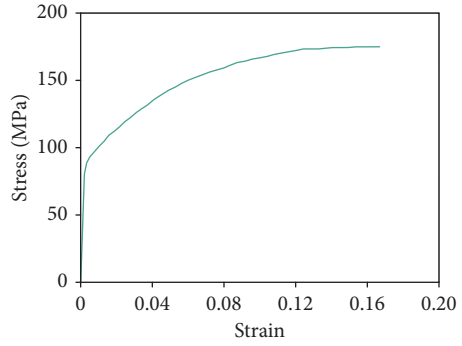

Figure 4: Engineering stress-strain curve of AA6060 T4 [17].

The rightmost columns of Tables 1–3 present the folding modes of each tube type, where CY, NCY, and NY indicate complete following, incomplete following, and no following of the pattern, respectively.

Convergence analysis for a reasonable mesh density was performed because a suitable mesh size is critical to accurate simulation of crushing behavior. For six models each of the two representative tubes, SQU and S6_R25_60, tube crushing was simulated using six mesh sizes from 1.2 to 3.0 mm, with the different numbers of elements and nodes, as illustrated in Figure 5(a). The resulting mean load for these models, illustrated in Figure 5(b), indicated that the results tended to converge when the mesh size was smaller than 2.0×2.0 mm. Therefore, to achieve the balance between computational efficiency and accuracy, an element size of 1.5×1.5 mm was adopted for all tubes. Although the same mesh size was adopted, the numbers of elements and nodes were inconsistent between specimens due to geometric differences. Element and node numbers were 35280–39440 and 35520–39516, respectively. The representative tubes of SQU had 35280 elements and 35520 nodes, whereas S6_R25_60 was modeled with 39360 elements and 39504 nodes.

Table 1: Geometries and numerical results of square tubes with patterns for the analysis of parameters M and θ.

Specimen	h (mm)	α (°)	Weight increase (%)	P_{max} (kN)	P_{max} reduction (%)	P_m (kN)	SEA (kJ/kg)	SEA increase (%)	Crushing trajectory
SQU	0.0	90.0	0	132.1	0	46.2	10.5	0	
S3_R25_88	1.0	88.4	0.1	71.2	46.1	45.2	10.3	−2.4	CF
S3_R25_84	2.9	85.1	0.4	65.3	50.6	44.7	10.1	−3.8	CF
S3_R25_80	4.8	81.8	0.7	58.0	56.1	44.5	10.1	−4.5	CF
S3_R25_76	6.9	78.5	1.2	55.5	58.0	43.8	9.9	−6.4	CF
S4_R25_88	0.7	88.8	0.1	87.2	34.0	49.4	11.2	6.7	NF
S4_R25_84	2.2	86.3	0.4	73.6	44.3	52.5	11.9	13.2	NCF
S4_R25_80	3.6	83.8	0.9	66.3	49.8	51.2	11.6	9.7	NCF
S4_R25_76	5.1	81.3	1.2	61.9	53.1	49.5	11.1	5.8	CF
S4_R25_72	6.7	78.8	1.4	61.0	53.8	48.6	10.9	3.6	CF
S5_R25_88	0.6	89.0	0.2	92.6	29.9	50.5	11.5	9.0	NF
S5_R25_84	1.7	87.1	0.7	77.1	41.6	49.2	11.1	5.7	NF
S5_R25_80	2.9	85.1	1.1	72.4	45.2	55.9	12.6	19.5	NCF
S5_R25_76	4.1	83.1	1.8	64.7	51.0	55.1	12.3	17.1	NCF
S5_R25_72	5.4	81.0	2.5	61.3	53.6	54.8	12.2	15.6	CF
S5_R25_68	6.7	78.8	3.0	59.7	54.8	53.5	11.8	12.4	CF
S5_R25_64	8.0	76.6	3.9	57.7	56.3	51.7	11.3	7.7	CF
S5_R25_60	9.5	74.2	4.5	57.4	56.5	50.3	11.0	4.1	CF
S6_R25_80	2.4	85.9	1.2	82.5	37.5	50.8	11.4	8.5	NF
S6_R25_76	3.4	84.2	1.9	80.5	39.1	50.9	11.4	8.0	NF
S6_R25_72	4.5	82.5	2.6	79.2	40.0	60.7	13.5	28.0	NCF
S6_R25_68	5.6	80.7	3.2	77.1	41.6	60.6	13.4	27.1	NCF
S6_R25_64	6.7	78.8	4.2	72.6	45.0	60.5	13.2	25.5	NCF
S6_R25_60	7.9	76.8	5.3	71.2	46.1	60.9	13.2	25.1	CF
S7_R25_76	2.9	85.0	1.9	83.4	36.9	51.3	11.5	8.8	NF
S7_R25_72	3.8	83.5	2.9	81.2	38.5	54.8	12.1	15.2	NF
S7_R25_68	4.8	82.0	3.7	79.4	39.9	61.1	13.4	27.5	NCF
S7_R25_64	5.7	80.3	4.6	73.5	44.4	62.5	13.6	29.2	NCF
S7_R25_60	6.8	78.6	5.6	70.3	46.8	60.4	13.0	23.8	NCF

4. Result Analysis

4.1. Crushing Response of Representative Tubes. Simulation of the SQU provided a benchmark to evaluate the crushing resistance of the designed patterned tubes; the resulting force-displacement curve is illustrated by black curves in Figure 6, and its corresponding crushing trajectory is illustrated in Figure 7(a). Here, the SQU regularly produced four layers and eventually collapsed into a typical symmetric quasi-inextensional mode, which is essentially consistent with previous experimental studies [8, 15]. The von Mises stress contour map of the undeformed pattern (see Figure 7(a)) indicates that plastic deformation majorly contributed to energy absorption, whereas the remaining areas showed limited involvement.

The theoretical mean load for the square tube subjected to low-velocity impact and deformed in quasi-inextensional mode can be expressed as follows [8, 9, 38, 39]:

$$P_m = 13.06 D_m \sigma_0 B^{1/3} t^{5/3}, \quad (5)$$

$$\sigma_0 = \sqrt{\frac{\sigma_y \sigma_u}{1+n}}, \quad (6)$$

where D_m is the dynamic amplification coefficient. Zhang et al. [20] and Tang et al. [40] proposed a value of 1.2, which was found to perform well in the prediction of the crushing responses of aluminum alloy AA6060 T4 square tubes under an axial dynamic impact with a velocity of 10 m/s, σ_0 is the equivalent plastic flow stress [17], and σ_y, σ_u, and n denote the initial yield strength, ultimate strength, and power-law exponent, respectively. Based on this formula, the mean load of SQU can be predicted as $P_m = 13.06 \times 1.2 \times 106 \times 90^{1/3} \times 3^{5/3} = 46.5$ kN, which is in good agreement with the numerical solution (46.2 kN).

Three representatives tubes, S6_R25_60, S6_R25_68, and S6_R25_76, all constituted by six modules, were selected to exhibit the deformation modes of square prefolded tubes as they had good crushing performances, and their folding processes had typical characteristics; their force-displacement curves are plotted in Figures 6(a)–6(c), respectively. Meanwhile, their resulting crushing trajectories and corresponding von Mises stress contour maps on undeformed patterns are shown in Figures 7(b)–7(d), respectively. Tube S6_R25_60 followed the pattern in a progressive and regular manner, as shown in Figure 7(b), and eleven layers of folds occurred on the tube, each accompanied by the activation of the inclined and horizontal plastic hinge lines. Compared with the four folding layers present in the SQU (see Figure 7(a)), S6_R25_60 had more regions involved in energy absorption, as is also evident in the last contour map in Figure 7(b), which shows large areas of plastic deformation. Comparison of the force-displacement curves of S6_R25_60 and the SQU, shown in Figure 6(a), with that of S6_R25_60

Table 2: Geometries and numerical results of the supplemental square patterned tubes for the analysis of ratio R.

Specimen	h (mm)	α (°)	Weight increase (%)	P_{max} (kN)	P_{max} reduction (%)	P_m (kN)	SEA (kJ/kg)	SEA increase (%)	Crushing trajectory
S5_R0_84	2.3	87.1	1.1	76.6	42.0	47.4	10.7	1.4	NF
S5_R0_80	3.9	85.1	1.7	70.7	46.5	55.7	12.5	18.5	NCF
S5_R0_76	5.5	83.1	2.3	64.3	51.3	54.6	12.2	15.5	NCF
S5_R0_72	7.1	81.0	2.8	60.0	54.6	52.1	11.6	9.7	CF
S5_R0_68	10.7	76.6	4.0	58.3	55.9	48.8	10.7	1.4	CF
S5_R25_84	1.7	87.1	0.9	77.1	41.6	49.3	11.1	5.7	NF
S5_R25_80	2.9	85.1	1.4	72.5	45.1	56.0	12.6	19.5	NCF
S5_R25_76	4.1	83.1	2.0	64.7	51.0	55.2	12.3	17.1	NCF
S5_R25_72	5.4	81.0	2.5	61.3	53.6	54.1	12.0	14.1	CF
S5_R25_68	6.7	78.8	3.0	59.4	55.0	53.2	11.8	11.8	CF
S5_R25_64	8.0	76.6	3.4	58.8	55.5	49.6	11.3	7.7	CF
S5_R50_84	1.2	87.1	0.9	79.5	39.8	48.5	11.0	4.0	NF
S5_R50_80	1.9	85.1	1.6	75.2	43.1	52.3	11.7	11.4	NF
S5_R50_76	2.7	83.1	2.6	65.5	50.4	55.4	12.3	16.9	NCF
S5_R50_72	3.6	81.0	3.0	62.9	52.4	54.4	12.0	14.3	NCF
S5_R50_68	4.4	78.8	4.4	61.4	53.5	54.0	11.8	12.0	CF
S5_R50_64	5.4	76.6	5.2	60.5	54.2	52.9	11.5	8.8	CF
S5_R75_72	1.8	81.0	3.6	81.0	38.7	49.1	10.8	2.7	NF
S5_R75_68	2.2	78.8	4.5	76.9	41.8	52.4	11.4	8.6	NF
S5_R75_64	2.7	76.6	5.1	73.2	44.6	54.5	11.8	12.3	NCF
S5_R75_60	3.2	74.2	6.0	64.3	51.3	53.8	11.6	9.9	NCF
S5_R75_56	3.7	71.7	6.9	63.3	52.1	53.2	11.3	7.7	NCF
S5_R75_52	4.3	69.1	7.0	59.4	55.0	52.8	11.3	6.9	CF
S6_R0_76	4.6	84.2	1.6	78.9	40.2	50.2	11.3	7.0	NF
S6_R0_72	5.9	82.5	2.9	76.6	42.0	58.8	13.0	23.7	NCF
S6_R0_68	7.4	80.7	4.4	73.3	44.5	57.0	12.5	18.3	NCF
S6_R0_64	8.9	78.8	6.4	70.8	46.4	55.8	12.0	13.5	NCF
S6_R0_60	10.6	76.8	8.8	66.7	49.5	55.5	11.6	10.5	CF
S6_R50_76	2.3	84.2	1.9	88.8	32.7	50.9	11.4	8.3	NF
S6_R50_72	3.0	82.5	2.1	85.1	35.5	53.5	11.9	13.4	NF
S6_R50_68	3.7	80.7	4.6	83.5	36.7	61.3	13.3	26.1	NCF
S6_R50_64	4.5	78.8	5.4	79.4	39.0	60.9	13.1	24.8	NCF
S6_R50_60	5.3	76.8	7.0	77.2	41.5	61.0	13.0	23.4	NCF
S6_R50_56	6.2	74.6	9.1	72.7	44.9	59.1	12.3	17.2	CF
S6_R75_48	4.1	69.8	8.7	76.2	42.3	51.5	10.8	2.6	NF
S6_R75_44	4.7	67.1	11.2	73.5	44.3	60.1	12.3	17.1	NCF
S6_R75_40	5.5	64.1	14.6	69.9	47.0	60.6	11.9	12.5	NCF
S6_R75_36	6.3	60.7	18.1	68.9	47.8	62.9	11.7	11.3	NCF
S6_R75_32	7.3	56.8	23.0	67.0	49.2	61.1	11.3	7.5	CF

demonstrates a gentler crushing process which is caused by the increase in folding number and shortening in folding wavelength. Furthermore, the removal of the high initial peak led to a significantly lower P_{max}. Although the crushing resistance of a single fold, which is indicated by the peak force, of S6_R25_60 was comparable to or slightly less than that present in those of the SQU, the excellent load consistency and stability led to an overall increase in the integral area of the curve, indicating that the energy absorption was considerably greater than that of the SQU. The resulting P_{max} and SEA of S6_R25_60 were 69.2 kN and 13.2 kJ/kg, respectively, representing a 47.6% decrease and a 25.1% increase, respectively, with respect to the SQU.

Predetermined modes were not always triggered. For example, as S6_R25_68, whose crushing trajectory is shown in Figure 7(c), was crushed, two layers did not follow the pattern, as indicated by the white dashed boxes. From the corresponding von Mises stress contour maps, however, the areas where high strain deformation occurred maintained a relatively uniform distribution and are still larger than that of the SQU, demonstrating an improved energy absorption. Accordingly, the load consistency of S6_R25_68 was superior to that of the SQU, as illustrated in Figure 6(b). The resulting SEA improved over that of the SQU by 27.1%, exceeding that of S6_R25_60. This variation between S6_R25_68 and S6_R25_60 was related to the change in θ and is discussed in Section 4.2.

Overall, the energy absorption only was improved significantly when the number of layers that adhered to the pattern during folding was at least two-thirds of the total number of layers. Thus, any tube meeting this criterion and for which the pattern was not completely followed was denoted as NCF. When the number of layers not adhering to the pattern rises above 1/3, the tubes tended to collapse into a

Table 3: Geometries and numerical results of the square prefolded tubes with various thicknesses.

	h (mm)	R	θ (°)	α (°)	t (mm)	B/t	P_{max} (kN)	P_m (kN)	Crushing trajectory
S6_1	7.9	0.25	60	76.8	3.0	30	71.2	60.9	CF
S6_2	7.9	0.25	60	76.8	2.5	36	41.1	38.2	CF
S6_3	7.9	0.25	60	76.8	2.0	45	28.1	25.2	CF
S6_4	7.9	0.25	60	76.8	1.5	60	18.3	15.4	CF
S6_5	7.9	0.25	60	76.8	1.0	90	9.5	6.9	CF
S6_6	7.9	0.25	60	76.8	0.75	120	5.6	4.0	CF

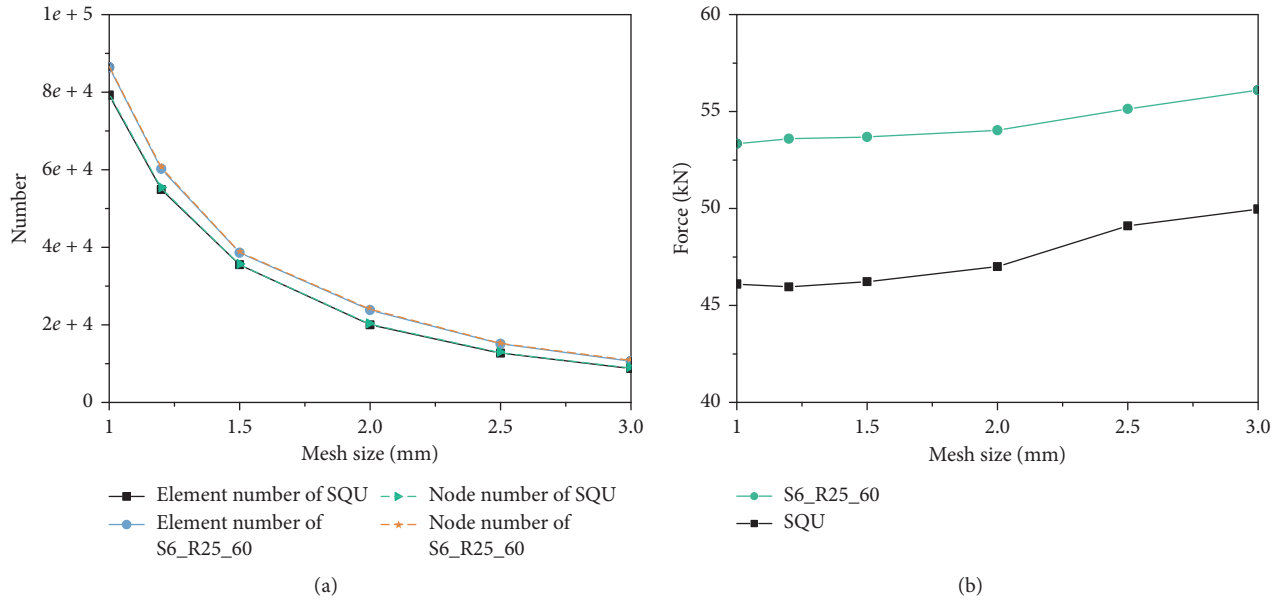

Figure 5: (a) Number of elements and nodes and (b) force convergence for two representative tubes with six mesh sizes.

noncompact mode with low performances and were thus denoted as NF; one such example is S6_R25_76, shown in Figure 7(d). Compared with those of S6_R25_60 and S6_R25_68, the von Mises stress contour maps of S6_R25_76 had fewer regions participating in strain deformation that were more unevenly distributed along the tube, leading to lower energy-absorption efficiency. Similarly, the response curve of S6_R25_76, presented in Figure 6(c), had fewer peaks and fluctuated more severely than that of the other two patterned tubes. Nevertheless, the load consistency of S6_R25_76 was still better than that of SQU, resulting in a slightly higher SEA (approximately 8.0% higher).

4.2. Effects of Key Parameters. First, the effects of parameters M and θ on the crushing responses of patterned tubes are analyzed. M represents the number of modules and thus determines the number of folding lobes. From a perspective of deformation, folding lobes act as the controller of folding waves. Prior research has confirmed that periodic imperfection structures, such as grooves [28], dents [29], and modular prefolded structures [30–35], can be used to control the folding wavelengths, thereby influencing the crushing mechanism. Furthermore, the presence of more modules in a tube may activate more plastic hinge lines, thus further improving energy absorption. However, the presence of too great a number of modules may complicate the tube structure and make the pattern hard to be followed.

As θ characterizes the steepness of the pyramidal patterning, it also influences the rotation of horizontal plastic hinge lines and the initial stiffness, thereby affecting the SEA and P_{max}. An increasing value of θ would reduce the inducibility of the predetermined deformation mode: with the increase in θ value, the defamation of the patterned tube would go through CF and NCF modes with high energy-absorption efficiency, and the NF mode accompanied by low efficiency would be triggered after exceeding a critical value of θ. However, a reducing θ is not conducive to crushing resistances, as it would reduce the rotation of the horizontal plastic hinge lines and reduce the corner angle φ (as determined in Figure 2(c)), which has been verified as a parameter positively related to the energy-absorption capacity of the square tube [8, 12]. The specific explanation is as follows: one fold of the square tube produces four two-panel folding elements, each of which consists of local energy-absorbing regions including a toroidal surface (E_1), two horizontal hinge lines (E_2), and two inclined hinge lines (E_3). The energies of those three types of energy dissipation contributors can be expressed as

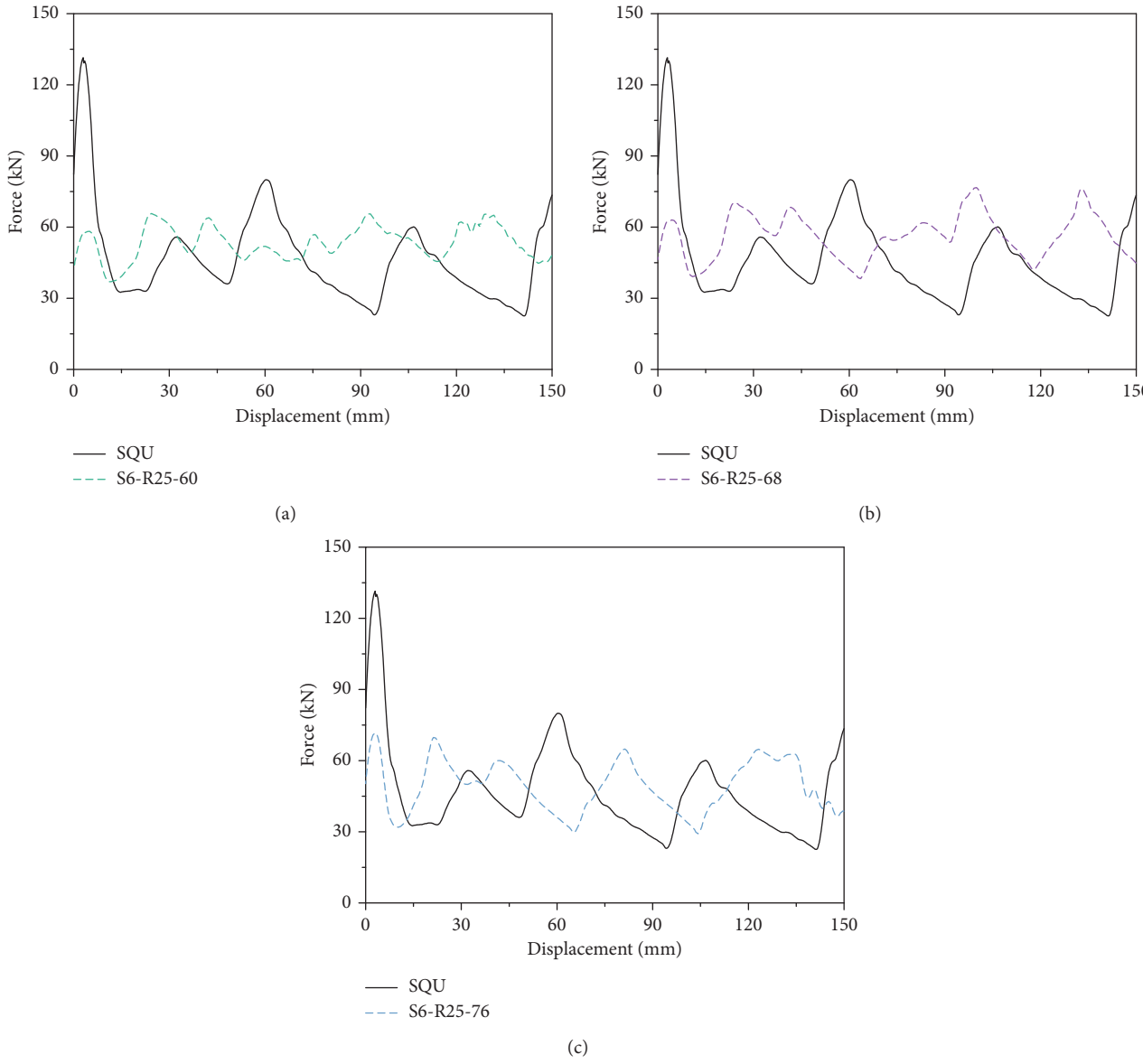

Figure 6: Comparison of force-displacement curves of SQU with (a) S6_R25_60, (b) S6_R25_68, and (c) S6_R25_76.

$$E_1 = 16M_0\frac{Hb}{t}I_1\left(\frac{\pi-\varphi}{2}\right),$$
$$E_2 = 2M_0B\theta, \tag{7}$$
$$E_3 = 2M_0\frac{H^2}{b}I_3\left(\frac{\pi-\varphi}{2}\right),$$

where M_0, H, t, B, and b denote the fully plastic bending moment, half folding wavelength, wall thickness, tube width, and the toroidal surface curvature of the square tube, respectively; I_1 and I_3 are two integral expressions related to the angle φ [8, 12], and θ is $\pi/2$ for square tubes with no prefolded pattern. Therefore, the absorbed energy of a two-panel folding element is $E = E_1 + 2E_2 + 2E_3$. A decrease in θ will decrease E_2, and according to [8, 12], a reduced φ caused by the decrease of θ is not conducive to the values of I_1 and I_3, thereby resulting in negative influences of E_1 and E_3.

Through the analysis and summary of numerical results in Table 1, the relationship between M and the resulting SEA and P_{max} is presented in Figures 8(a) and 8(b), respectively, and the relationship between θ and the resulting SEA and P_{max} is illustrated in Figures 8(c) and 8(d), respectively. Here, SEA and P_{max} are normalized with those of the SQU. Seven specimens, highlighted by red circles in Figures 8(a)–8(d), collapsed without following the pattern. For $M = 4$, 5, 6, and 7, the resulting critical value of θ was thus 88°, 84°, 76°, and 72°, respectively. Thus, as M increased, the critical value of θ decreased. During deformation, the SQU folded into four layers axially, thus representing the natural deformation mode of the tube; according to the principle of minimum energy [12], this mode corresponds to the minimum energy

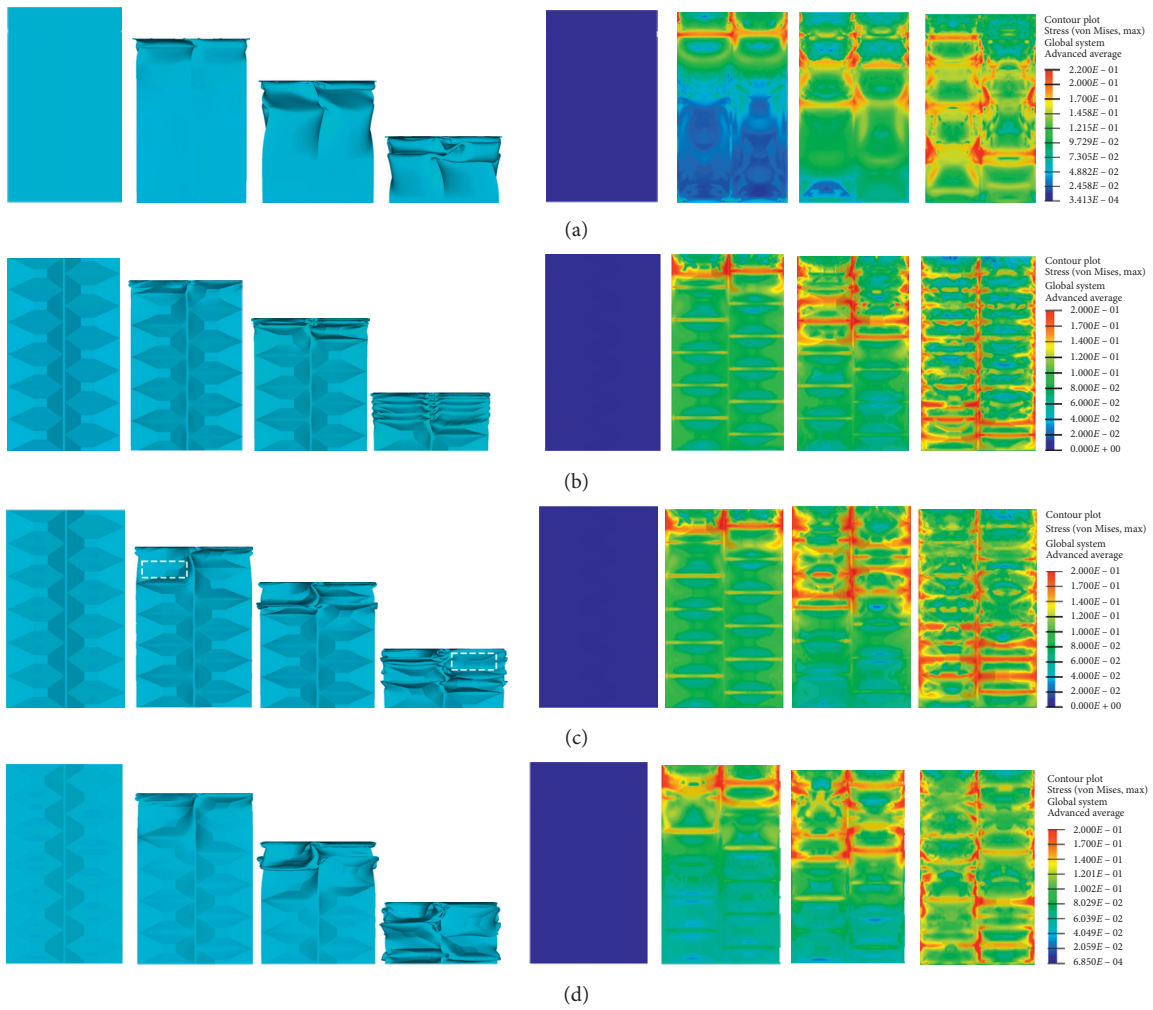

FIGURE 7: Crushing processes (left) and corresponding von Mises stress contour maps on undeformed patterns (right) of (a) the traditional square tube (SQU), (b) S6_R25_60, (c) S6_R25_68, and (d) S6_R25_76.

and the most stable deformation manner. Hence, as M approaches four, the deformation mode tends toward stability. As M is increased and the number of folds deviates further from the natural model, the pattern becomes more difficult to be followed. Overall, three main conclusions were drawn:

As θ and M increase, the tubes become less likely to collapse into predetermined modes.

At constant θ, increases to M lead to an increase in both the SEA and P_{max}. However, a dramatic slump in the SEA occurred when the pattern was not followed, whereas this trend was not observed in P_{max}, indicating that P_{max} is insensitive to the deformation mode.

At constant M, P_{max} increases with increasing θ, regardless of the deformation mode, whereas the SEA increases with increasing θ, except when deformation patterns are not followed.

Overall, high values of M and θ enhance the energy-absorption efficiency, but reduce the likelihood of generating the predetermined deformation modes.

Second, to analyze the effect of R on the crushing responses, patterned tubes with $M = 5$ and 6 and four values of R (0, 0.25, 0.5, and 0.75) were modeled. The numerical results are listed in Table 2 and the resulting relationships between R and the normalized SEA and P_{max} are plotted in Figures 8(e)–8(h).

The data presented in Table 2 indicate that, when M and θ remain unchanged, P_m increases with increasing R until the NF mode occurs. For instance, at $M = 5$ and $\theta = 68^\circ$, as R increased from 0 to 0.5, P_m increased from 48.8 to 54.0 kN, but when R reached 0.75, the NF mode was triggered and P_m decreased to 52.4 kN. Moreover, when $M = 6$ and $R = 0.75$, the θ range in which the reasonable deformation mode can be triggered was 32°–44°, which diverged from that of the tubes with $R = 0$, 0.25, and

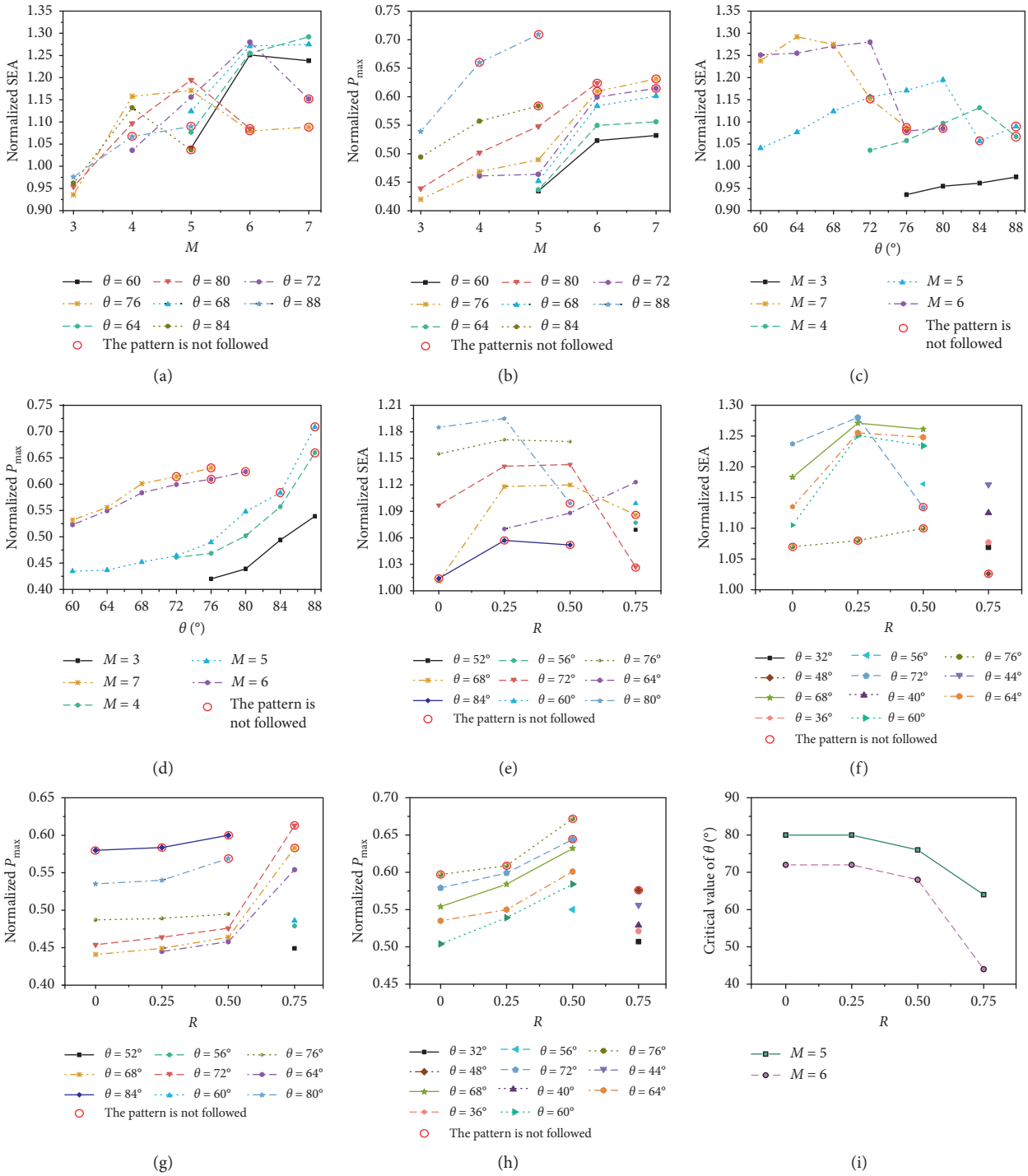

FIGURE 8: Relationship between the (a) normalized SEA and M, (b) normalized P_{max} and M, (c) normalized SEA and θ, (d) normalized P_{max} and θ, normalized SEA and R at (e) $M = 5$ and (f) $M = 6$, normalized P_{max} and R at (g) $M = 5$ and (h) $M = 6$, and (i) the critical value of θ and R for square patterned tubes.

0.50 (56°–72°). Therefore, observing continuous changes in P_m with increasing R (from 0 to 0.75) at a certain θ value is impossible, but it is possible in the R interval 0–0.5, such as is observed for the conditions of $\theta = 60°$, 64°, and 68°. Nevertheless, the increase in P_m did not yield a continuous increase in the SEA, as illustrated in Figures 8(e) and 8(f). Reasons are as follows: first, when θ and M were constant, with the increase in R, the occurrence of NF mode led to a sharp decrease in the SEA, such as $M = 5$, $\theta = 80°$, and $M = 6$, $\theta = 72°$; second, an increased R led to the increase of the mass, and when the increasing extent of the mass exceeded that of the P_m, it eventually led to the decrease in the SEA, according to equation (4).

As shown in Figures 8(g) and 8(h), P_{max} increased with an increasing R although not linearly. Generally, the growth rate of P_{max} was relatively slow from $R = 0$ to 0.25, whereas when $R > 0.5$, it began to accelerate, as illustrated in Figure 8(g) ($M = 5$). For $M = 6$, although for the reasons mentioned above, it is difficult to observe the continuous change in P_{max} in the R interval of 0–0.75. Nevertheless, a similar trend can be observed in R from 0 to 0.5 (see Figure 8(h)).

Additionally, for $M = 5$, $R = 0$, 0.25, 0.50, and 0.75, the critical value of θ was 84°, 84°, 80°, and 68°, respectively, thereby demonstrating a decreasing critical value of θ with increasing R, as summarized in Figure 8(i). The same trend was also observed at $M = 6$. High values of R thus made the pattern more difficult to follow; this was further verified by comparing the deformation modes of four representative tubes ($M = 5$ and $\theta = 72°$) with varying R values, as shown in Figure 9. When $R \leq 0.25$, CF modes were triggered. When $R = 0.5$, an irregular fold appeared on the tube, as indicated by the white dashed box. When $R = 0.75$, the tube collapsed into the NF mode. This trend is easy to explain: when M and θ are constant, the increase in R will decrease the pyramid height h. If the pyramids are regarded as alternative indentation triggers, the gradual shallowing of those triggers will reduce the inducibility of the predetermined deformation mode. Moreover, the increase in R improves the buckling strength of the structure, as discussed above, which, coupled with the previous reason, eventually led to the pattern being difficult to follow.

Therefore, tubes with a patterning in which $R \leq 0.25$ are more inclined to deform following the pattern. Considering the SEA, deformation mode, and P_{max}, $R = 0.25$ is regarded as the optimal value among the interval of 0 to 1 and was thus used during the analysis presented in Sections 4, and 5.

Finally, as the ratio B/t governs the folding pattern of a conventional tube, variation of this ratio can cause the tube to fold in different patterns, thus varying performance parameters. B/t also has a significant impact on tubes with prefolded pattern. For example, the patterned tube designed by Zhang et al. [30] was very sensitive to the change in B/t, only in a small value range of which the predetermined deformation mode can be activated. This limits the application of the structure as it is very common to adjust the thickness of the tube to meet different energy-absorption requirements in engineering cases. Therefore, six tubes were established based on the same geometry as S6_R25_60 with $3.0 \geq t \geq 0.75$ mm (i.e., $30 \leq B/t \leq 120$) and investigated; the results of these six square prefolded tubes, S6_1–S6_6, are listed in Table 3. Additionally, the deformation modes of these tubes are plotted in Figure 10.

The deformation modes of the six studied prefolded tubes were not influenced by the variation in B/t and the folding pattern was consistently followed. Therefore, the deformation mode of the designed square tube with pyramidal patterning is insensitive to variations in the ratio B/t, which is a desirable characteristic in designing thin-walled structures and can make the crushing process controllable.

5. Structural Improvement

5.1. Octagonal Tube with Pyramidal Patterning. According to the previous analysis, two defects were present in the square pyramidal patterned tube. First, the structure with a high value of θ or M led the pattern hard to be followed. Second, SEA enhancement of each square patterned tube did not exceed 30%, as there are significant limitations in enhancing the energy-absorption capacity due to only improving the load consistency but not adding local plastic energy-absorbing regions of each single fold. Therefore, the structural compliance and energy-absorption performance of the structure need to be improved.

To increase the number of local plastic energy-absorbing regions, four basic pyramids were added to the square module to make it octagonal, as illustrated in Figure 11, which activated more inclined plastic hinge lines in a single fold. Assuming that the developed eight-cornered module collapses into the predetermined mode, the number of inclined plastic hinge lines increases from four pairs to eight pairs, a half of which are denoted by orange dotted lines in Figure 11, thus greatly improving the energy-absorption efficiency.

To explore the energy-absorption capacity of the improved structure, octagonal tubes with pyramidal patterning and the traditional octagonal tube (OCT) were modeled using the above method mentioned in Section 3. The key dimensions of those tubes were as follows: tube length $L = 220.0$ mm, thickness $t = 3.0$ mm, and edge width $c = 45.0$ mm, and the geometric parameters of the pyramid elements of octagonal patterned tubes are listed in Table 4. Note that $R = 0.25$ was adopted by all octagonal patterned tubes as it was the optimal value according to the previous analysis. Additionally, the naming system of octagonal patterned tubes adopted the same logic as their square counterparts. For instance, O6_R25_84 indicated an octagonal patterned tube with six modules, and values of R and θ were 0.25 and 84°, respectively.

Crushing tests were numerically simulated with the same load conditions of square tubes, and crushing responses are summarized in Table 4. Comparative analysis was then conducted.

5.2. Comparative Analysis. The resulting crushing trajectory and corresponding von Mises stress contour maps on undeformed patterns of the OTC and a representative octagonal prefolded tube that collapsed following CF, O6_R25_80 (selected as the optimal design), are presented in Figures 12(a) and 12(b), respectively. Additionally, their resulting load-displacement curves are compared with that of the conventional square tube, SQU, in Figure 13. The OTC progressively collapsed with six annular folds and eventually deformed into concertina mode. A large annular strain region with extension deformation occurred, as shown in the contour map of Figure 12(a), leading to an evidently enhanced energy-absorbing efficiency of the OTC, and its SEA was 16.2 kJ/kg, approximately 53.9% higher than that of the SQU. However, the sharp fluctuation and high P_{max}

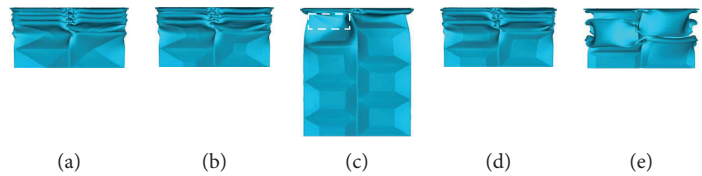

Figure 9: Deformation modes of four representative square prefolded tubes with different values of R: (a) S5-R0-72; (b) S5-R25-72; (c) S5-R50-72; (d) S5-R75-72.

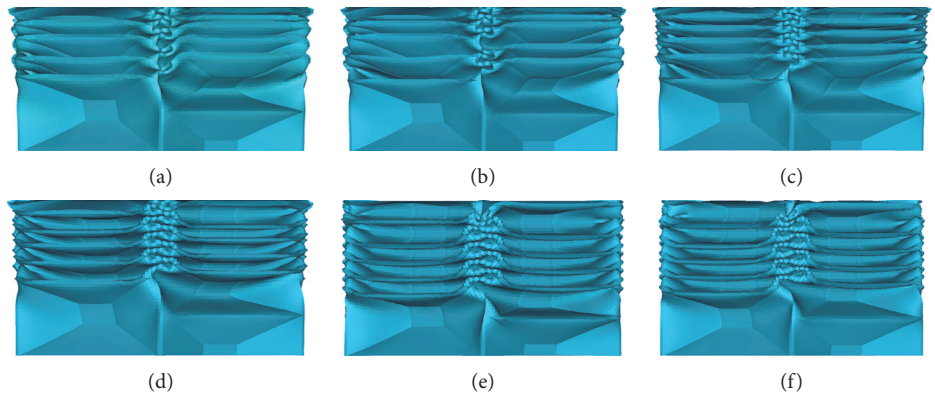

Figure 10: Deformation modes of the square prefolded tubes with various values of B/t. (a) S6_1 ($t = 3$ mm). (b) S6_2 ($t = 2.5$ mm). (c) S6_3 ($t = 2.0$ mm). (d) S6_4 ($t = 1.5$ mm). (e) S6_5 ($t = 1.0$ mm). (f) S6_6 ($t = 0.75$ mm).

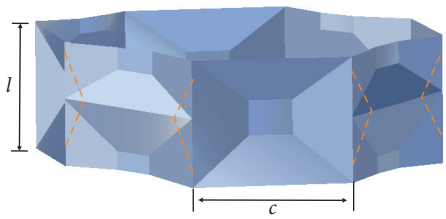

Figure 11: Illustration of a single module of the prefolded patterned tube with an octagonal profile.

(137.3 kN) of the response curve of the OTC indicate that there is still room for improvement.

A more progressive and stable deformation process, including complete following of the pattern, was observed for O6_R25_80, shown in Figure 12(b). The introduction of the octagonal profile increases the number of inclined plastic hinge lines from four pairs in each module in the square configuration to eight pairs in the new structure while maintaining the total length of horizontal plastic hinges. This indicates that the efficient diamond model was triggered [31]; as a result, a greater area participated in high strain deformation, as illustrated by the von Mises stress contour maps. Furthermore, the load curve of O6_R25_80 (see Figure 13) demonstrated similar advantages of the designed square patterned tubes, including a stable loading process and short folding wavelength, which combined with the increased inclined plastic hinge lines, further improved crushing performances. Overall, the SEA of O6_R25_80 was 19.9 kJ/kg, representing an increase over that of the SQU and OTC of 89.7% and 23.2%, respectively, and the P_{max} was 120.1 kN, representing a decrease from that of the SQU and OTC of 9.1% and 12.5%, respectively. Thus, the developed patterned octagonal tube is more desirable as an energy-absorption device than the traditional square and octagonal tubes.

To verify the performance improvements of patterned tubes brought by the introduction of octagonal profiles, square prefolded tubes S6_R25_60–S6_R25_80 were compared with octagonal counterparts studied containing the same t, M, and cross-sectional perimeter, O6_R25_72–O6_R25_86. The resulting SEA and P_{max} as a function of θ are compared in Figures 14(a) and 14(b), respectively. Here, the SEA of the octagonal prefolded tubes was integrally higher than that of their square counterparts to approximately 1.5 times, indicating that the additional inclined plastic hinge lines were successfully activated by introducing octagonal profiles. A similar increase was also observed in the resulting P_{max}, and increasing the value of θ gradually amplified the difference of P_{max}; this inevitable increase in P_{max} of the octagonal prefolded tubes was accompanied, however, by a tremendous improvement in crushing resistance.

Moreover, the critical values of θ of the square and octagonal prefolded tubes with values of M from 3 to 6 are compared in Figure 14(c). Obviously, the octagonal patterned tube has an advantage over its square counterpart in the critical values of θ, and with an increase in M, the advantage gradually increased. Therefore, octagonal patterned tubes were easier to collapse into the predetermined mode than their square counterparts under the condition of high values of M and θ, indicating that the octagonal prefolded

Table 4: Geometries and numerical results of traditional and prefolded octagonal tubes.

	c (mm)	h (mm)	α (°)	Weight increase	P_{max} (kN)	P_{max} reduction (%)	P_m (kN)	SEA (kJ/kg)	SEA increase (%)	Crushing trajectory
OTC	45	0.0	90.0	0.0	137.3	−3.9	71.1	16.2	53.9	—
O3_R25_89	45	0.5	88.4	0.0	124.8	5.5	81.6	18.6	76.5	NCF
O3_R25_88	45	1.0	86.7	0.2	121.2	8.3	80.9	18.4	74.6	CF
O4_R25_89	45	0.4	88.8	0.0	126.1	4.5	86.0	19.6	86.0	NCF
O4_R35_88	45	0.7	87.6	0.2	122.4	7.3	82.9	18.9	79.0	CF
O5_R25_89	45	0.3	89.0	0.0	130.0	1.6	86.4	19.7	86.8	NCF
O5_R25_88	45	0.6	88.0	0.2	124.2	6.0	83.6	19.0	80.4	CF
O6_R25_86	45	1.0	86.7	0.6	127.2	3.7	86.5	19.6	86.0	NF
O6_R25_84	45	1.4	85.1	1.0	124.4	5.8	88.8	20.0	90.1	NCF
O6_R25_80	45	2.4	81.8	1.7	120.1	9.1	89.2	19.9	89.7	CF
O6_R25_76	45	3.4	78.5	2.5	106.1	19.7	85.0	18.9	79.3	CF
O6_R25_72	45	4.5	75.2	3.5	92.6	29.9	84.9	18.7	77.4	CF

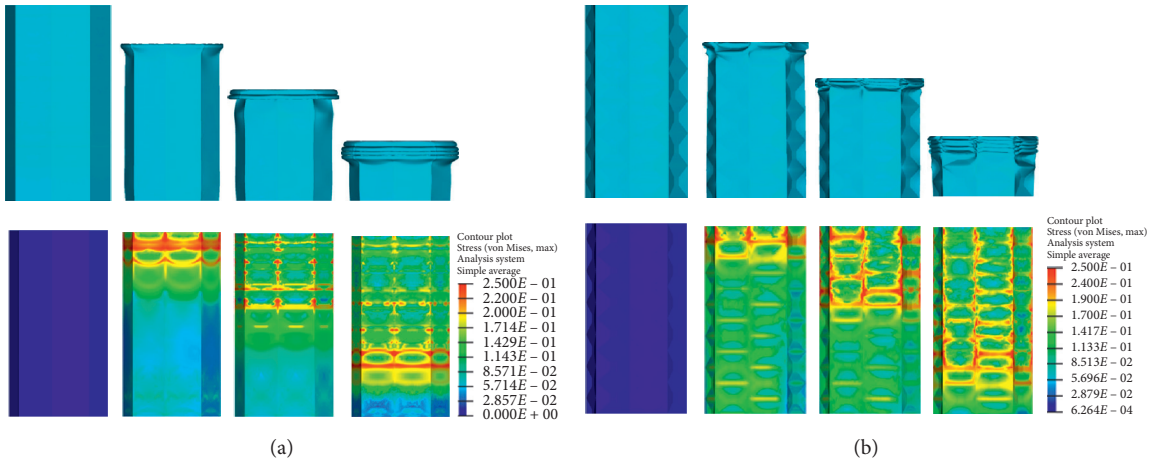

(a) (b)

Figure 12: Crushing processes (top) and corresponding von Mises stress contour maps on undeformed patterns (bottom) of (a) OTC and (b) O6_R25_80.

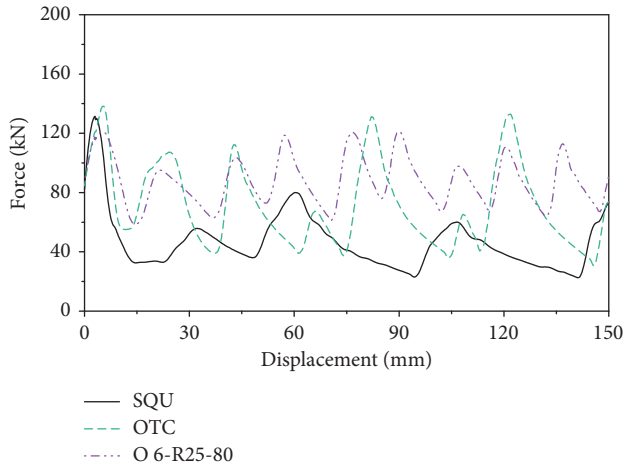

Figure 13: Force-displacement curves of the traditional square and octagonal tubes and the proposed octagonal prefolded tube.

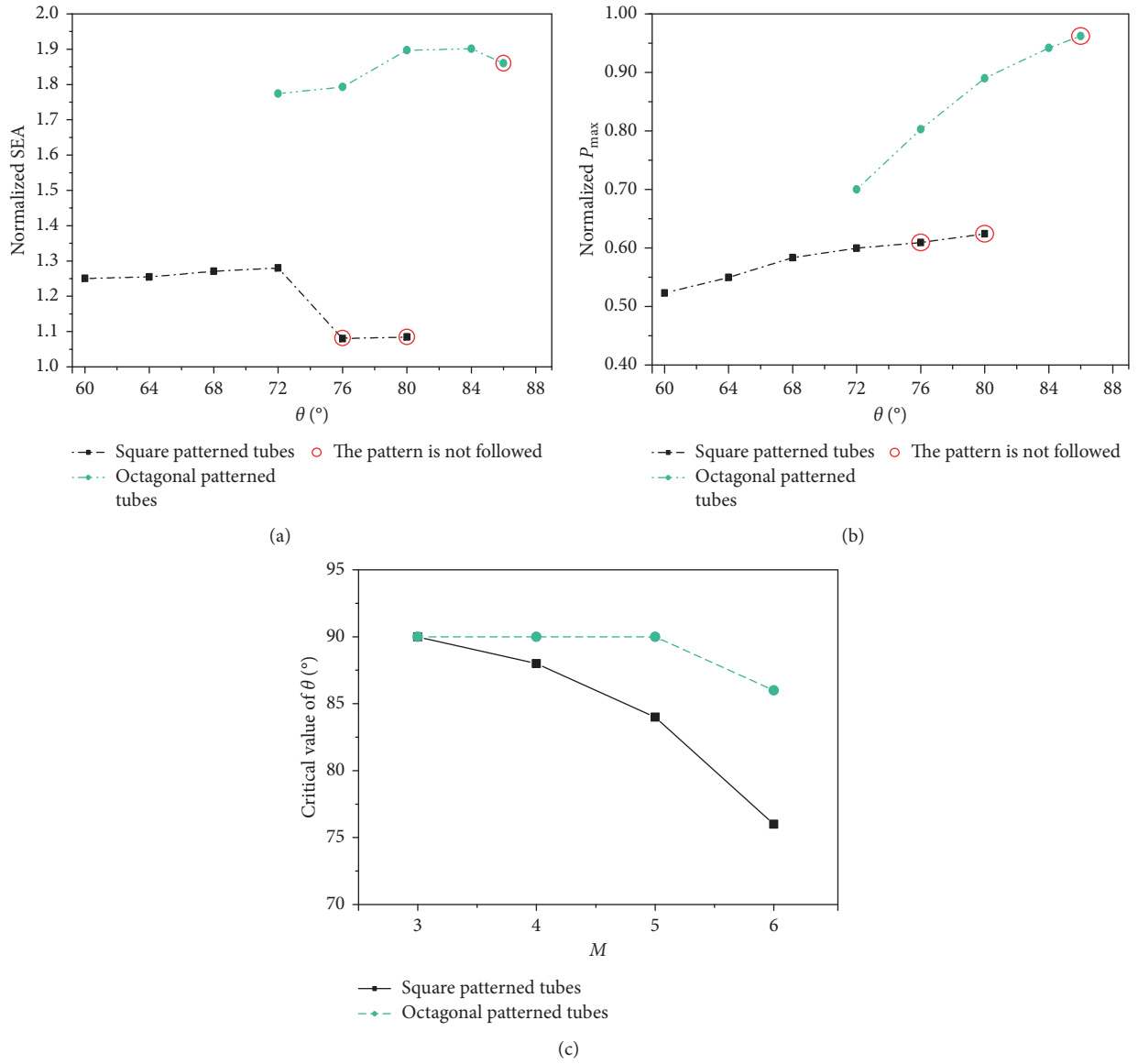

FIGURE 14: Relationship between the (a) normalized SEA and θ, (b) normalized P_{max} and θ, and (c) critical value of θ and M for square and octagonal tubes with patterning.

tubes have better pattern compliance than do the square counterparts.

Therefore, octagonal tubes with pyramidal patterning are superior to similarly patterned square tubes in terms of crushing performances.

6. Conclusions

In this work, a type of prefolded tube with improved pyramidal patterns was designed to realize multiperformance enhancement, including deformation mode control, inhibition of the maximum peak load, and increase in energy-absorption efficiency. A series of specimens were simulated to evaluate the crushing performance improvement caused by pattern implementation and to investigate the effects of crucial geometric parameters and sectional profiles on crushing responses. The nonlinear FE code LS-DANA/ANSYS was employed to simulate the collapse behaviors of tubes subjected to dynamic crush; simulation results revealed that the multiperformance enhancement was effectively realized. Geometric and comparative analyses based on the simulation results were then performed. The following conclusions were then drawn:

Parameters M and θ are crucial in controlling the deformation mode of patterned tubes and influencing the P_{max} and SEA. Specifically, the low values of M and θ help induce predetermined deformation modes

whereas the high values of M and θ can increase the SEA, given that the deformation pattern is followed. Moreover, increases in M and θ can lead to an increase in P_{max}.

Higher values of R improve SEA but decrease the likelihood of predetermined deformation modes being induced, and they also increase P_{max}. The threshold value of θ, which designates the occurrence of a nonpredetermined mode, decreases with increasing R. An optimal value of $R = 0.25$ was determined for the range of parameters studied.

Finally, the comparative analysis indicated that employing patterned octagonal tubes rather than square tubes causes a remarkable increase in the SEA and significantly improve structural compliance, while the excellent P_{max} inhibition is still maintained. In addition, notable multiperformance improvements are also present when comparing the patterned octagonal and traditional tubes.

Overall, the designed octagonal patterned tube is the superior structure and thus the most crashworthy among the tubes studied. Future work will aim to experimentally study the patterned tubes presented in the present work and verify advantages in their performance.

Notations

L:	Initial length of tube
B:	Width of square tube
c:	Edge width of octagonal tube
t:	Wall thickness
φ:	Corner angle of tube, defined in Figure 2(c)
M:	Module number of patterned tubes
R:	Ratio of top to bottom area of pyramid
l:	Height of an individual module
p:	The longer side length of pyramid top
s:	The shorter side length of pyramid top
h:	Height of pyramid element
α and θ:	Angles between bottom normal and side plates of pyramid, defined in Figure 1
V:	Impact velocity of striking mass
M_0:	Fully plastic bending moment
σ_0:	Equivalent plastic flow stress (see ref. [17])
σ_y:	Initial yield strength
σ_u:	Ultimate strength
n:	Power-law exponent
m:	Tube mass
δ:	Effective crushing distance
P_m:	Crushing force
P_{max}:	Maximum peak force
SEA:	Specific energy absorption defined in equation (4)
E_1, E_2, and E_3:	Internal energy absorption defined in equation (7)
H:	Half folding wavelength of tube
b:	Toroidal surface curvature (see refs. [8, 9])
I_1 and I_3:	Integrals related to φ (see refs. [8, 9])
D_m:	Dynamic amplification coefficient.

Data Availability

The data used to support the findings of this study are available from the corresponding author upon request.

Conflicts of Interest

The authors declare that there are no conflicts of interest regarding the publication of this paper.

Acknowledgments

This work was supported by the Science and Technology Research and Development Plan of China State Railway Group Co., Ltd. (grant no. N2020J027).

References

[1] J. M. Alexander, "An approximate analysis of the collapse of thin cylindrical shells under axial loading," *The Quarterly Journal of Mechanics and Applied Mathematics*, vol. 13, no. 1, pp. 10–15, 1960.

[2] T. Wierzbicki, S. U. Bhat, W. Abramowicz, and D. Brodkin, "Alexander revisited-A two folding elements model of progressive crushing of tubes," *International Journal of Solids and Structures*, vol. 29, no. 24, pp. 3269–3288, 1992.

[3] A. A. Singace, H. Elsobky, and T. Y. Reddy, "On the eccentricity factor in the progressive crushing of tubes," *International Journal of Solids and Structures*, vol. 32, no. 24, pp. 3589–3602, 1995.

[4] A. Pugsley, "The large-scale crumpling of thin cylindrical columns," *The Quarterly Journal of Mechanics and Applied Mathematics*, vol. 13, no. 1, pp. 1–9, 1960.

[5] A. G. Pugsley, "On the crumpling of thin tubular struts," *The Quarterly Journal of Mechanics and Applied Mathematics*, vol. 32, no. 1, pp. 1–7, 1979.

[6] A. A. Singace, "Axial crushing analysis of tubes deforming in the multi-lobe mode," *International Journal of Mechanical Sciences*, vol. 41, no. 7, pp. 865–890, 1999.

[7] G. Lu and T. X. Yu, *Energy Absorption of Structures and Materials*, CRC-Woodhead, Cambridge, UK, 2003.

[8] T. Wierzbicki and W. Abramowicz, "On the crushing mechanics of thin-walled structures," *Journal of Applied Mechanics*, vol. 50, no. 4, pp. 727–734, 1983.

[9] W. Abramowicz and N. Jones, "Dynamic axial crushing of square tubes," *International Journal of Impact Engineering*, vol. 2, no. 2, pp. 179–208, 1984.

[10] W. Abramowicz and N. Jones, "Transition from initial global bending to progressive buckling of tubes loaded statically and dynamically," *International Journal of Impact Engineering*, vol. 19, no. 5-6, pp. 415–437, 1997.

[11] W. Abramowicz and T. Wierzbicki, "Axial crushing of multicorner sheet metal columns," *Journal of Applied Mechanics*, vol. 56, no. 1, pp. 113–120, 1989.

[12] W. Abramowicz, "Thin-walled structures as impact energy absorbers," *Thin-Walled Structures*, vol. 41, no. 2-3, pp. 91–107, 2003.

[13] M. Yamashita, M. Gotoh, and Y. Sawairi, "Axial crush of hollow cylindrical structures with various polygonal cross-sections," *Journal of Materials Processing Technology*, vol. 140, no. 1–3, pp. 59–64, 2003.

[14] X. Zhang and H. Huh, "Crushing analysis of polygonal columns and angle elements," *International Journal of Impact Engineering*, vol. 37, no. 4, pp. 441–451, 2010.

[15] X. Zhang and H. Zhang, "Energy absorption of multi-cell stub columns under axial compression," *Thin-Walled Structures*, vol. 68, pp. 156–163, 2013.

[16] X. Zhang and H. Zhang, "Experimental and numerical investigation on crush resistance of polygonal columns and angle elements," *Thin-Walled Structures*, vol. 57, pp. 25–36, 2012.

[17] S. P. Santosa, T. Wierzbicki, A. G. Hanssen, and M. Langseth, "Experimental and numerical studies of foam-filled sections," *International Journal of Impact Engineering*, vol. 24, no. 5, pp. 509–534, 2000.

[18] W. Chen and T. Wierzbicki, "Relative merits of single-cell, multi-cell and foam-filled thin-walled structures in energy absorption," *Thin-Walled Structures*, vol. 39, no. 4, pp. 287–306, 2001.

[19] X. Zhang and G. Cheng, "A comparative study of energy absorption characteristics of foam-filled and multi-cell square columns," *International Journal of Impact Engineering*, vol. 34, no. 11, pp. 1739–1752, 2007.

[20] X. Zhang, G. Cheng, and H. Zhang, "Theoretical prediction and numerical simulation of multi-cell square thin-walled structures," *Thin-Walled Structures*, vol. 44, no. 11, pp. 1185–1191, 2006.

[21] A. Najafi and M. Rais-Rohani, "Mechanics of axial plastic collapse in multi-cell, multi-corner crush tubes," *Thin-Walled Structures*, vol. 49, no. 1, pp. 1–12, 2011.

[22] Z. Wang, J. Liu, and S. Yao, "On folding mechanics of multi-cell thin-walled square tubes," *Compos Part*, vol. B2018, no. 132, pp. 17–27.

[23] F. Xu, X. Tian, and G. Li, "Experimental study on crashworthiness of functionally graded thickness thin-walled tubular structures," *Experimental Mechanics*, vol. 55, no. 7, pp. 1339–1352, 2015.

[24] J. Zhou, R. Qin, and B. Chen, "Energy absorption properties of multi-cell thin-walled tubes with a double surface gradient," *Thin Walled Struct*, vol. 145, 2019.

[25] X. Zhang, Z. Wen, and H. Zhang, "Axial crushing and optimal design of square tubes with graded thickness," *Thin-Walled Structures*, vol. 84, pp. 263–274, 2014.

[26] J. Zhou, R. Qin, and B. Chen, "On the folding mechanics of square columns with double-surfaced gradients," *Mathematical Problems in Engineering*, vol. 2019, p. 16, 2019.

[27] A. A. Singace and H. El-Sobky, "Behaviour of axially crushed corrugated tubes," *International Journal of Mechanical Sciences*, vol. 39, no. 3, pp. 249–268, 1997.

[28] G. H. Daneshi and S. J. Hosseinipour, "Grooves effect on crashworthiness characteristics of thin-walled tubes under axial compression," *Materials & Design*, vol. 23, no. 7, pp. 611–617, 2002.

[29] S. Lee, C. Hahn, M. Rhee, and J.-E. Oh, "Effect of triggering on the energy absorption capacity of axially compressed aluminum tubes," *Materials & Design*, vol. 20, no. 1, pp. 31–40, 1999.

[30] X. Zhang, G. Cheng, Z. You, and H. Zhang, "Energy absorption of axially compressed thin-walled square tubes with patterns," *Thin-Walled Structures*, vol. 45, no. 9, pp. 737–746, 2007.

[31] J. Ma and Z. You, "Energy absorption of thin-walled square tubes with a pre-folded origami pattern-part I: geometry and numerical simulation," *Journal of Applied Mechanics*, vol. 81, no. 1, 2014.

[32] C. Zhou, B. Wang, J. Ma, and Z. You, "Dynamic axial crushing of origami crash boxes," *International Journal of Mechanical Sciences*, vol. 118, pp. 1–12, 2016.

[33] J. Ma, D. Hou, Y. Chen, and Z. You, "Quasi-static axial crushing of thin-walled tubes with a kite-shape rigid origami pattern: numerical simulation," *Thin-Walled Structures*, vol. 100, pp. 38–47, 2016.

[34] C. Zhou, Y. Zhou, and B. Wang, "Crashworthiness design for trapezoid origami crash boxes," *Thin-Walled Structures*, vol. 117, pp. 257–267, 2017.

[35] K. Yang, S. Xu, J. Shen, S. Zhou, and Y. M. Xie, "Energy absorption of thin-walled tubes with pre-folded origami patterns: numerical simulation and experimental verification," *Thin-Walled Structures*, vol. 103, pp. 33–44, 2016.

[36] W. Lv, D. Li, and L. Dong, "Study on blast resistance of a composite sandwich panel with isotropic foam core with negative Poisson's ratio," *International Journal of Mechanical Sciences*, vol. 191, 2021.

[37] H. Xin, J. A. F. O. Correia, and M. Veljkovic, "Three-dimensional fatigue crack propagation simulation using extended finite element methods for steel grades S355 and S690 considering mean stress effects," *Engineering Structures*, vol. 227, 2021.

[38] A. G. Hanssen, M. Langseth, and O. S. Hopperstad, "Static and dynamic crushing of square aluminum extrusions with aluminum foam filler," *International Journal of Impact Engineering*, vol. 24, no. 5, pp. 347-348, 2000.

[39] M. Langseth and O. S. Hopperstad, "Static and dynamic axial crushing of square thin-walled aluminium extrusions," *International Journal of Impact Engineering*, vol. 18, no. 7-8, pp. 949–968, 1996.

[40] Z. Tang, S. Liu, and Z. Zhang, "Energy absorption properties of non-convex multi-corner thin-walled columns," *Thin-Walled Structures*, vol. 51, pp. 112–120, 2012.